

# Long Term Study of Sedimentation and Biofouling at Cascadia Basin, the Site of the Pacific Ocean Neutrino Experiment

O. Aghaei<sup>1</sup>, M. Agostini<sup>2</sup>, S. Agreda<sup>1</sup>, A. Alexander Wight<sup>2</sup>,  
 P. S. Barbeau<sup>3,4</sup>, A. J. Baron<sup>1</sup>, S. Bash<sup>5</sup>, C. Bellenghi<sup>5</sup>, B. Biffard<sup>1</sup>,  
 M. Boehmer<sup>5</sup>, M. Brandenburg<sup>5</sup>, D. Brussow<sup>1</sup>, N. Cedarblade-Jones<sup>3,4</sup>,  
 M. Charlton<sup>1</sup>, B. Crudele<sup>2</sup>, M. Danninger<sup>6</sup>, F. C. De Leo<sup>1,7</sup>, T. DeYoung<sup>8</sup>,  
 F. Fuchs<sup>9</sup>, A. Gärtner<sup>6</sup>, J. Garriz<sup>8</sup>, D. Ghuman<sup>6</sup>, L. Ginzkey<sup>5</sup>,  
 V. Gousy-Leblanc<sup>5</sup>, D. Grant<sup>6</sup>, A. Grimes<sup>6</sup>, C. Haack<sup>10</sup>, R. Halliday<sup>9</sup>,  
 D. Hembroff<sup>1</sup>, F. Henningsen<sup>6</sup>, J. Hutchinson<sup>1</sup>, R. Jenkyns<sup>1</sup>, S. Karanth<sup>11</sup>,  
 T. Kerscher<sup>5</sup>, S. Kershtein<sup>1</sup>, K. Kopański<sup>11</sup>, C. Kopper<sup>10</sup>, P. Krause<sup>6</sup>,  
 C. B. Krauss<sup>12</sup>, I. Kulin<sup>1</sup>, N. Kurahashi<sup>13</sup>, C. Lagunas Gualda<sup>5</sup>, A. Lam<sup>1</sup>,  
 T. Lavallee<sup>1</sup>, K. Leismüller<sup>5</sup>, R. Li<sup>5</sup>, S. Loipolder<sup>5</sup>, A. Magaña Ponce<sup>9</sup>,  
 S. Magel<sup>5</sup>, P. Malecki<sup>11</sup>, G. G. Marshall<sup>2</sup>, T. Martin<sup>12</sup>, S. Mihaly<sup>1</sup>,  
 C. Miller<sup>6,14</sup>, N. Molberg<sup>12</sup>, R. Moore<sup>12</sup>, B. Nührenbörger<sup>5</sup>, B. Nichol<sup>6</sup>,  
 W. Noga<sup>11</sup>, R. Ørsøe<sup>5</sup>, L. Papp<sup>5</sup>, V. Parrish<sup>8</sup>, M. Paulson<sup>1</sup>, P. Pfahler<sup>5</sup>,  
 B. Pirenne<sup>1</sup>, E. Price<sup>1</sup>, A. Rahlin<sup>15,16</sup>, M. Rangen<sup>12</sup>, E. Resconi<sup>5</sup>,  
 C. Ridsdale<sup>1</sup>, S. Robertson<sup>12</sup>, A. Round<sup>1</sup>, D. Salazar-Gallegos<sup>8</sup>, A. Scholz<sup>5</sup>,  
 L. Schumacher<sup>10</sup>, S. Sharma<sup>11</sup>, C. Spannfellner<sup>5</sup>, J. Stacho<sup>6</sup>, I. Taboada<sup>17</sup>,  
 A. R. Thurber<sup>18</sup>, M. Tradewell<sup>1</sup>, J. P. Twagirayezu<sup>8</sup>, M. Un Nisa<sup>8</sup>,  
 B. Veenstra<sup>12</sup>, S. Wagner<sup>1</sup>, C. Weaver<sup>8</sup>, N. Whitehorn<sup>8</sup>, L. Winter<sup>5</sup>,  
 M. Wolf<sup>1</sup>, R. Wroński<sup>11</sup>, J. H. Wynne<sup>18</sup>, J. P. Yañez<sup>12</sup>, A. Zaalishvili<sup>3,4</sup>,

<sup>1</sup>Ocean Networks Canada, University of Victoria, Victoria, BC, Canada

<sup>2</sup>Department of Physics and Astronomy, University College London, Gower Street, London, WC1E 6BT, UK

<sup>3</sup>Department of Physics, Duke University, Durham, NC, 27708, USA

<sup>4</sup>Triangle Universities Nuclear Laboratory, Durham, NC, 27708, USA

<sup>5</sup>Physik-department, Technische Universität München, D-85748 Garching, Germany

<sup>6</sup>Department of Physics, Simon Fraser University, 8888 University Drive Burnaby, B.C. Canada, V5A 1S6

<sup>7</sup>Department of Biology, University of Victoria, Victoria BC V8N 1V8, Canada

<sup>8</sup>Department of Physics and Astronomy, Michigan State University, East Lansing, MI 48824, USA

<sup>9</sup>Department of Physics, Elmhurst University, 190 S. Propsect Ave, Elmhurst, IL, 60126, USA

<sup>10</sup>Erlangen Centre for Astroparticle Physics, Friedrich-Alexander-Universität Erlangen-Nürnberg, D-91058 Erlangen, Germany

<sup>11</sup>Institute of Nuclear Physics, Polish Academy of Sciences, Kraków, Poland

<sup>12</sup>Department of Physics, University of Alberta, Edmonton, Alberta, Canada, T6G 2E1

<sup>13</sup>Department of Physics, Drexel University, 3141 Chestnut Street, Philadelphia, PA, 19104, USA

<sup>14</sup>Department of Physics and Astronomy, University of Victoria, 3800 Finney Road, Victoria, BC, Canada, V8P 5C2

<sup>15</sup>Department of Astronomy and Astrophysics, University of Chicago, 5640 South Ellis Avenue, Chicago, IL, 60637, USA

<sup>16</sup>Kavli Institute for Cosmological Physics, University of Chicago, 5640 South Ellis Avenue, Chicago, IL, 60637, USA

<sup>17</sup>School of Physics and Center for Relativistic Astrophysics, Georgia Institute of Technology, Atlanta, GA 30332, USA

<sup>18</sup>Department of Ecology, Evolution, and Marine Biology, University of California, Santa Barbara, CA, USA

the date of receipt and acceptance should be inserted later

**Abstract** We present a study of the effects of biofouling and sedimentation on pathfinder instrumentation for the Pacific-Ocean Neutrino Experiment (P-ONE), which will be located in the Cascadia Basin region of the North Pacific Ocean. P-ONE will look for high-energy neutrinos by observing the light produced when these neutrinos interact in the water, detecting and digitiz-

ing single photon signals in the ultraviolet-visible range. We measure that biofouling and sedimentation caused a decrease in the transparency of upward-facing optical surfaces over 5 years of operations. A majority of downward-facing optical surfaces, which will dominate P-ONE's sensitivity to astrophysical sources, showed no visible biofouling. Extrapolations motivated by biological growth models estimated that these losses started around 2.5 years after deployment, and suggest a final

<sup>a</sup>e-mail: btveenst@ualberta.ca

equilibrium transparency ranging between 0% and 35% of the original for the upward-facing modules.

## 1 Introduction

The Pacific-Ocean Neutrino Experiment (P-ONE) is a cubic kilometre scale neutrino telescope that is under development, to be deployed at a depth of 2660 m in the Cascadia Basin in the North Pacific Ocean [1]. The P-ONE scientific collaboration is partnered with Ocean Networks Canada (ONC) and will use their NEPTUNE infrastructure, which consists of over 800 km of fiber-optic and power cables connecting undersea research nodes [2]. The P-ONE instrumentation will be connected to a node in the Cascadia Basin. This region is located in a flat segment of an abyssal plain on the Juan de Fuca plate, around 200 km off the coast of Vancouver Island in Canada.

Neutrino telescopes are used to study the neutrino sky [1, 3, 4]. This is accomplished by observing the light produced by secondary charged particles when neutrinos interact in the water [5]. An array of optical instruments equipped with photomultiplier tubes (PMTs), called optical modules, are used to instrument a volume of water and coincident observation of photons among multiple PMTs enables neutrino detection. Energy deposited in the detector is estimated based on the total amount of light measured and neutrino flavour identification can be approached based on the spatial characteristics of the observed light.

Using this detection principle requires that the attenuation length of the water is long enough that it is technologically and economically feasible to build a large detector. In order to measure the optical properties of the water, the P-ONE collaboration deployed the STRings for Absorption length in Water (STRAW) pathfinder in the summer of 2018 [6]. The measurements made by the STRAW instrument qualified the Cascadia Basin as a suitable site for a full scale detector [7]. The background rate distribution of ambient light due to bioluminescence was measured and monitored by STRAW since March 2019 [7, 8]. A second pathfinder, STRAW-b, was deployed in 2020 [9, 10]. Both pathfinder instruments were successfully recovered in the summer of 2023. A schematic of the STRAW apparatus is shown in Fig. 1.

Any instrumentation deployed in the ocean environment for long periods of time will be affected by the buildup of marine sediments and biological material, effects collectively known as fouling. The five years during which the STRAW apparatus was deployed allowed for the measurement of fouling and its effects on detector performance.

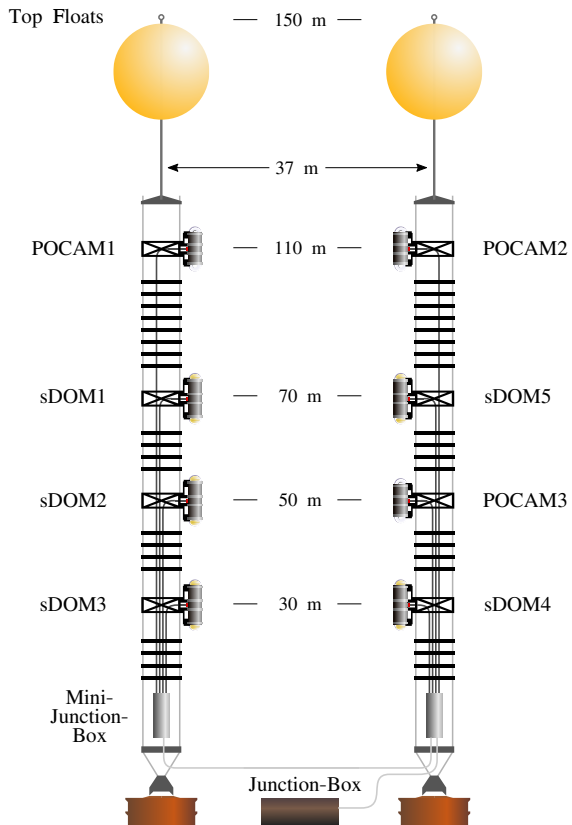


Fig. 1: The STRAW instrument [6, 7]. Precision Optical CALibration Module (POCAM) modules consisted of different wavelength diodes that could be pulsed at known voltages and acted as flasher beacons [11]. The STRAW Digital Optical Module (sDOM)s acted as light collecting modules and consisted of an upward- and downward-facing PMT. Figure reproduced from Ref. [7] with kind permission of the European Physical Journal (EPJ).

Marine fouling is caused primarily by three effects and their interactions. Sedimentation refers to inorganic and organic materials vertically sinking from the water column into the seabed [12, 13]. Secondly, a flux of larger particulate aggregates known as marine snow that is composed of detritus, living organisms, organic and inorganic matter, is also transported down from the surface ocean towards the seabed [14, 15]. Marine snow and sedimentation will be referred to interchangeably, because they both have an equivalent effect of depositing material on submerged surfaces. The third process, known as biological fouling or biofouling, refers to living organisms that colonize submerged surfaces [16, 17, 18].

Sedimentation and biological fouling present a concern to neutrino telescopes because the PMTs view the

water through a pressure resistant glass housing. Material buildup eventually makes this glass less transparent, reducing telescope sensitivity. This effect is strongest on upward-facing surfaces [19].

The genetic diversity of fouling organisms has previously been found to depend strongly on depth and moderately on substrate orientation [20]. The longest such study was done by the ANTARES collaboration, in the Mediterranean Sea [21]. This study found a 20% average reduction in optical transparency and 15% detector efficiency reduction over nine years [22]. The ANTARES optical modules faced downwards at a 45° angle, and were located at depths between 2100 m and 2375 m [21, 23]. ANTARES modules had a reduced exposure to marine snow relative to a surface that was not facing partially downwards.

The STRAW apparatus was visually surveyed three times by means of video from a remotely operated vehicle (ROV) deployed from a surface vessel. The first inspection was done in 2018, shortly after deployment. A second survey of STRAW was performed in 2020, showing some evidence of material buildup on top of the optical modules [8, 24]. A third and final survey was done in 2023, just before recovery, that showed an established biofouling population. Figure 2 shows the progression of buildup on an individual module.

Measurements of the evolution of the transmission efficiency from STRAW show a decline over the detector’s lifetime for the upward-facing modules [25]. In this work, the evolution of the transmission efficiency for selected modules are presented using the full 53 month data set. A discussion on insights from the recovery and possible mitigation strategies is then presented.

## 2 Measuring the Transparency of STRAW Optical Modules

### 2.1 Detector and Data Selection

The STRAW instrument consisted of two mooring lines with four instrument modules each, as shown in Fig. 1. Precision Optical CALibration Modules (POCAMs) acted as light flashing beacons and contained a precision diffusing sphere with a set of four light-emitting diodes (LED) operating at 365, 405, 465 and 605 nm wavelengths [11]. The remaining STRAW Digital Optical Module (sDOM)s each contained two PMTs, one upward-facing towards the surface and the other downward-facing towards the sea-floor [6].

The STRAW detector had two data taking modes. A low-precision mode counted the number of times each PMT was triggered in 30 ms intervals and operated

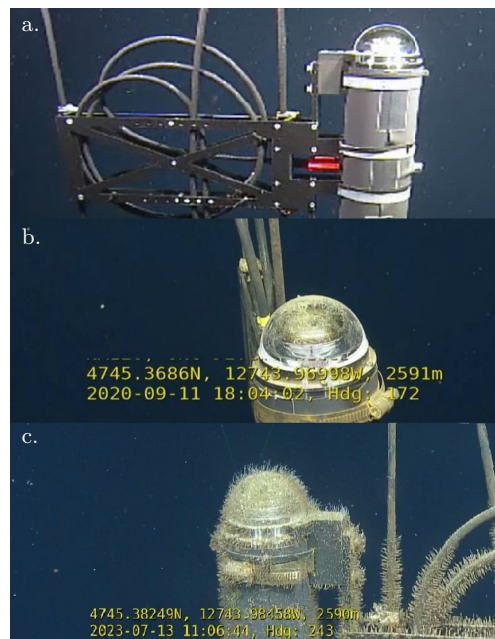


Fig. 2: Image of an optical module that was part of the STRAW apparatus. The module is shown clean shortly after deployment in 2018 (a.). An amount of buildup is visible in the 2020 survey (b.). The final 2023 survey shows a developed macro-fouling population, composed primarily of hydroids (c.).

continuously [7]. The number of PMT triggers was converted into a rate. Data from this mode were stored as both a time series, and as histograms of the distribution of rates in one hour intervals, the latter of which were used for this study. An alternative high-precision mode could record time over threshold measurements with sub-nanosecond precision using a time-to-digital converter (TDC) and was run in dedicated campaigns [6, 7]. Between March 2019 and July 2023, STRAW took data continuously in the slow mode with a fractional up-time of 98.3% in its first two years of operation [7]. Across the full 53 month data set, the fractional up-time increased to 99.5%.

Data taking periods where the POCAM was active were initiated by specifying an intensity (voltage), flasher frequency, and LED wavelength. The data set used for this study consisted of new measurements taken specifically for the purpose of measuring the efficiency evolution of the optical modules, as well as archival data from previous studies. The majority of archival data had the POCAM set to use the 465 nm LED flashing at a frequency of 2.5 kHz and the intensity set to the maximum of 20 V. New measurements were taken matching these flasher conditions. To compensate for the saturation of the PMT nearest the POCAM, the

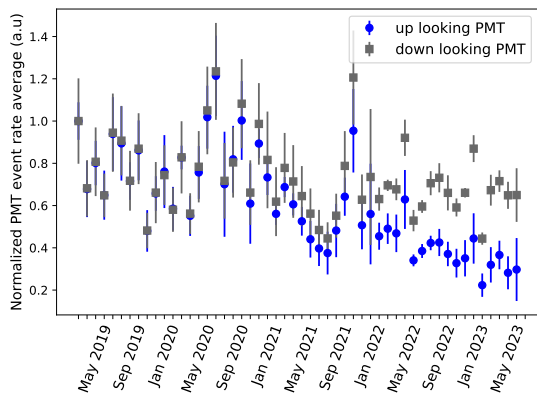


Fig. 3: Relative PMT trigger rates seen by both upward-facing and downward-facing optical surfaces in STRAW due to ambient light sources, such as bioluminescence. The total light was averaged monthly across all upward- and downward-facing PMTs, and then normalized to March 2019. On large time scales, fluctuations in the light measured are observed in correlation between orientations.

relative efficiencies for the highest sDOM were measured using flashes from the POCAMs on the opposing mooring line.

## 2.2 Method Using Low-Precision STRAW Data

The purpose of the low-precision data taking mode was to measure the rate of background light in the future P-ONE site [7]. A broad range of rates extending from a few kHz to rates above the data-acquisition (DAQ) sampling limit of 10 MHz were observed [7]. The lowest observed rates were around 10 kHz and are attributed to light emissions from decays of radioisotopes present in the ocean water, mainly potassium-40, and the intrinsic dark rate of the PMTs [7]. Very high rates are attributed to the activity of bioluminescent organisms [7].

Bioluminescent rates have seasonal variations, which were seen in the STRAW data [7]. Figure 3 shows that large monthly fluctuations are consistent between upward-facing and downward-facing PMT rates.

The majority of downward-facing module surfaces showed little to no visible fouling. Both optical modules positioned 70 m above the seafloor were clear of visible biofouling on the downward-facing glass, one of which can be seen in Fig. 4. sDOM3’s downward-facing surface was also observed to be free of visible fouling, at an elevation of 30 m above the sea-floor. The downward-facing flasher modules, located 110 m above the seafloor, were both observed to be free from

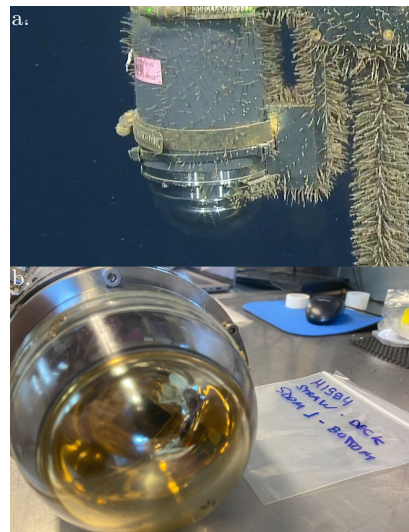


Fig. 4: STRAW sDOM1 during the ROV survey (a.) and on deck after recovery (b.), showing an unobstructed downward-facing optical surface.

visible fouling. sDOM2 and sDOM4 at 50 m and 30 m above the sea floor did show visible biofouling on the underside. Data from these two modules were excluded from this study, as the method described below could not be used to measure their efficiency over time. The glass housings of the uppermost POCAM, facing down at 110 m above the seafloor, were observed to be free of visible fouling.

Correlation between rates in up and down looking PMTs due to ambient light, combined with the clean downward-facing glass observed in several modules implies that the ratio

$$R = \frac{\langle N_{\text{light}} \rangle_{\text{upper}}}{\langle N_{\text{light}} \rangle_{\text{lower}}}, \quad (1)$$

is a good estimator for the evolution of the transmission efficiency of the upward-facing optical surfaces. In equation 1  $N_{\text{light}}$  is the average light seen in the binning period, and the average ratio,  $R$ , was computed monthly for the top most optical modules and one of two modules nearest the seafloor. The result of this  $R$  measurement is shown in the shaded areas in Fig. 5 where the thickness of the band indicates the  $1\sigma$  confidence interval. As a cross check, a selection of fast data was used to independently compute this ratio and found to be compatible with the results shown in Fig. 5.

## 2.3 High-Precision Method and Results

Flasher data taking periods used the high-precision DAQ mode. In order to estimate the light collection efficiency,

while accounting for attenuation in the water, the fraction of POCAM flashes detected was calculated based on the flasher rate and the measured number of flashes in a one second integration window. The phase of the time synchronization between the POCAM and the sDOM was computed using the same method as Ref. [7]. This method was not based on both PMTs in a module, and therefore wasn't affected by biofouling on the downward-facing PMT.

Only high-precision data where the noise rate was below 100 kHz was used. This cut-off rate was chosen to minimize the chance of a noise hit due to the ambient bioluminescence light occurring in coincidence with the flasher, while retaining a large fraction of the data. In cases where part of an integration window had a background rate above the 100 kHz limit, the high rate portion was excluded and the expected number of flashes was recalculated based on the length of the time window remaining. Data taking periods using the flasher were thirty seconds to one minute long, resulting in 60 nominally one-second integration windows. These 60 measurements were averaged, with the standard error on the mean taken as the statistical error, to compute a data point for each flasher-data-taking period.

A persistent decrease in the ratio of detected flashes over time was measured. The results of the different flasher data are shown as points in figure 5. In order to normalize the two different data sets and estimate systematic errors, a scaling factor was fit to the high-precision data. The resulting uncertainty from this scaling process was propagated onto the high-precision data points. The fraction of flashes detected by a PMT depends on the attenuation length of the water and distance from the light source. Distance from the light source is affected by ocean currents, and attenuation length may be influenced by seasonal variations in sediment content [26,27]. Both are related to tidal effects and therefore expected to be periodic, not continuously decreasing as observed in Fig. 5. We therefore attribute this loss in transmission efficiency to the accumulation of biofouling and sedimentation that was observed in visual surveys of the STRAW instrument.

### 3 Time Dependence of Fouling Effects

The long term behavior is driven by biological effects, which is supported by key observations made during the recovery of the STRAW apparatus. A variety of models and approaches for describing the growth of cells and populations exist in the literature [28]. Most models follow sigmoid shapes and are characterized by three phases: an initial phase with slow growth, an exponential transition and a final state of slow growth where the

population asymptotically approaches a limit. A selection of models from the literature were fit to the optical data shown in Fig. 5.

A subset of these, the Richards family of models, have been used to analyze a variety of different biological systems [29]. Model selection was assessed on three criteria: goodness of fit, magnitude of uncertainties, and the behavior of models near boundaries. Based on this, two models from the Richards family emerged as candidates, the Logistic and Gompertz models described in Ref. [29] and Ref. [30]. These models are defined by three parameters: the inflection time  $T_i$ , the relative growth rate at inflection  $k_{rel}$ , and asymptotic population limit or carrying capacity,  $P_\infty$ .

Population limit refers to a maximum size or maximum number of the individual units that make up the population. The 2023 ROV survey identified the larger invertebrates making up the biofouling to be hydroids (Cnidaria: Hydrozoa). A subsequent analysis of samples identified an assortment of microbial, as well as inorganic and organic non-living material. The STRAW apparatus could not be used to count these entities individually. Instead, the assumption was made that the transmission efficiency would decrease in proportion to the accumulated material:

$$\eta(t) = 1 - \alpha P(t), \quad (2)$$

where  $\alpha$  is a constant of proportionality and  $P_\infty$  is the asymptotic population limit. The product of  $\alpha$  and  $P_\infty$  can be fit, we define this as a new parameter

$$A = \alpha P_\infty, \quad (3)$$

representing the fraction of the optical surface that would be obscured by fouling in the long term limit. Applying Eq. 2 and 3 to the functional form of the Logistic model from Ref. [29] gives:

$$\eta(t) = 1 - \frac{A}{1 + e^{-k_{rel}(t-T_i)}}. \quad (4)$$

Doing the same for the Gompertz model from Ref. [30]:

$$\eta(t) = 1 - Ae^{-k_{rel}(t-T_i)}. \quad (5)$$

A value of  $\alpha=1.0$  implies that the surface becomes opaque in the asymptotic limit. This is not a hard limit and it is possible for the value of  $A$  to converge to a value larger than 1.0, as the underlying behavior being modeled is growth on top of a glass substrate. This would occur in a case where the glass becomes completely obscured before the fouling population reaches an equilibrium state.

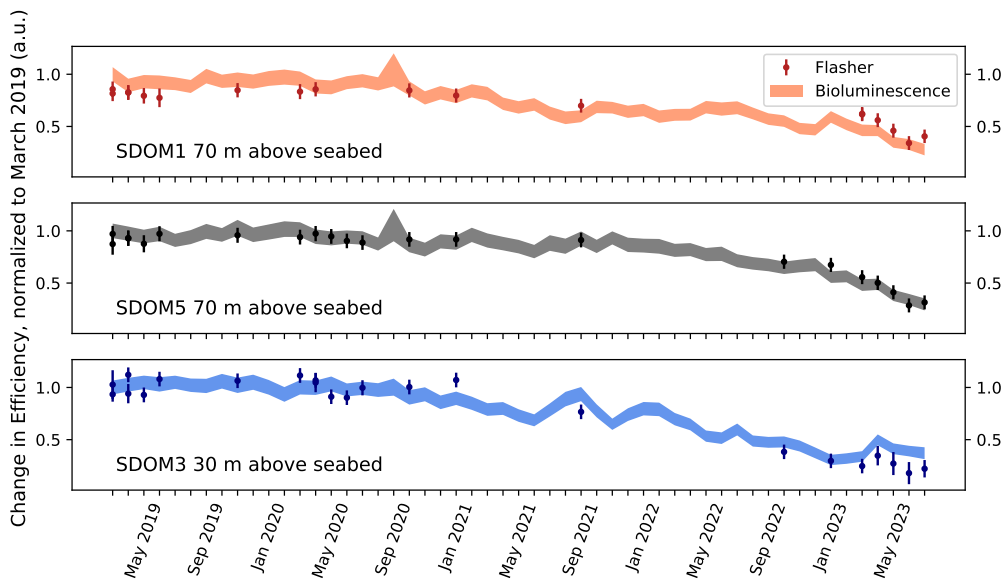


Fig. 5: Evolution of the light transmission efficiency of selected upward-facing module surfaces. The shaded region shows the one sigma confidence interval for the ratio obtained using ambient bioluminescence light. Individual points show the results of direct measurements using the flasher. All data is normalized to March 2019, and a scaling factor is used between the two data sets to account for different systematic uncertainties between the two methods.

The rate,  $k_{\text{rel}}$  described by this parametrization refers to a relative growth rate [29]. This can be converted to an absolute growth rate,  $k_{\text{foul}}$ , using the equation:

$$k_{\text{foul}} = \left. \frac{\partial P}{\partial t} \right|_{t=T_i} = c_m A k_{\text{rel}} \quad (6)$$

where it can be shown that  $c_m$  is a model dependent constant for each of the models described in [29].  $c_m$  takes a value of  $e^{-1}$  for the Gompertz model and  $1/4$  for the Logistic model. Absolute growth rate may be understood as the maximum rate that the population grows at, or in this case the maximum rate of loss of transmission efficiency. In this work, maximum growth rate is referred to as the fouling rate and is reported for both models in Table 1.

Fitting was accomplished by maximizing a likelihood function, assuming Gaussian errors on the STRAW measurements. Additional assumptions were made that the resulting likelihood estimators for the three parameters are efficient, and that the number of data points are sufficient to be in the large sample limit. Under these conditions, the inverse of the covariance matrix may be estimated by computing the second derivative of the log-likelihood function. The inverse of the resulting matrix can then be taken to get the uncertainty on each of the parameters.

The likelihood fitting process was used to fit each model to a combined data set of the three sDOMs for

which complete data sets exist. This combined data set was computed by taking the weighted average and variance of each of the sDOM data sets shown in Fig. 5. A resampling based on each model was performed in order to estimate a likelihood distribution and calculate a p-value for that model. Analysis of the individual sDOMs showed stochastic fluctuations that were accounted for in the sampling by taking an average of the deviations on each month of data.

Both of the models considered in the final analysis can be approximated by a linear fit about the inflection point. This line was extrapolated to the point where it intersects with a line indicating no change in efficiency. The time associated with this point is used to calculate a parameter that will be referred to as the critical time.

$$T_c = - \frac{1 - (\eta(T_i) - T\eta'(T_i))}{\eta'(T_i)}. \quad (7)$$

We chose to define the critical time this way in order to estimate where the optical data transitioned from steady to a decline, while accounting for the fact that different models were applied. The efficiency of each model was evaluated at the critical time and found to be around 90% for both the Gompertz and Logistic models. On future instruments, monitoring when the transparency of optical surfaces fall below 90% of their

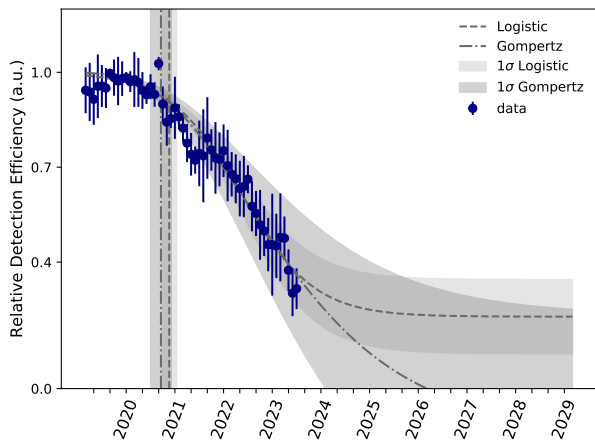


Fig. 6: Fit of the logistic and Gompertz models to the combined data from Fig. 5. Rates of fouling are shown for each model and are in good agreement with each other. The vertical dashed and dashed-dotted lines represent the calculated critical times, and the shaded bands around these lines indicate the corresponding  $1\sigma$  confidence interval. Another confidence interval is shown around the expected maximal transparency loss. The fit is extrapolated in order to show the asymptotic behaviour of the fits and because future P-ONE strings are being designed for a minimal operation time of 10 years.

value at immersion can be used as an indicator of entering the rapid-growth phase.

The critical time and fouling rate were calculated for the combined data set using each fitted model. Information from the fits is summarized in Table 1. Each model showed an acceptable goodness of fit based on the calculated p-values. The critical times are shown with errors in the shaded horizontal bands on Fig. 6, which suggests that the growth rates predicted by each model are compatible. These growth rates suggest a maximum annual loss in transparency of around 25% per year shortly after the critical time has been reached. STRAW had been deployed for 8 months when regular data taking started, so this result implies that rapid efficiency losses take hold at around the two and a half year mark. Using the upper  $1\sigma$  limit on  $A$  in Table 1 and using Fig. 6, we can extrapolate the asymptotic behaviour of the biofouling. The final transparency of the upward-facing glass ranges from 0% to 35% of the initial value in the long term limit.

## 4 Sampling of Biofouling and Sedimentation

During the recovery of the two STRAW pathfinder instruments, samples were taken of the biofouling and sediment that had accumulated. These samples were taken from various points on each instrument. In-water sampling was done using a suction collection system connected to a holding area (suction sampler) on the ROV. Additional samples were taken onboard the deck of the recovery vessel.

The placement of instrumentation on the first STRAW pathfinder was shown in Fig. 1 [6, 7]. Suction samples were taken from the tops of sDOM1 and sDOM5, located at 70 m above the seafloor. No samples were taken of the bottom of these modules, as they appeared to be free of biofouling. Samples were taken both on the top and bottom of sDOM2, where biofouling was present.

STRAW-b was a 450 m tall mooring line, which was equipped with several different types of modules for making environmental measurements. The purposes and general layout of these instruments can be found in Fig. 2. of Ref. [10]. Suction samples were taken from the tops of the modules positioned at 432 m, 144 m, and 120 m above the sea floor.

The objective of taking samples was to identify the microbial component, known as the biofilm, of the accumulated biofouling. Identifying these could lead to mitigation strategies for biofouling, which will improve the long term light collection efficiency of upward-facing modules. Figure 7 shows the microbial families identified on sampled modules.

DNA was extracted from the biofilm samples using the Zymobiomics DNA miniprep kit (Zymo Research, Irvine, CA). Polymerase chain reaction (PCR) amplification was carried out according to the protocols of the Earth Microbiome Project (see Ref. [31]) following Ref. [32]. Amplicons were sequenced on an Illumina MiSeq (V.2 chemistry and 2x250 paired-end sequencing) by Oregon State University’s Center for Quantitative Life Sciences (CQLS). Sequences were quality-filtered by FASTP using default settings [33]. 16S analysis was carried out on forward reads using the Qiime2 Dada2 wrapper to predict Amplicon Sequence Variants (ASVs) [34], using the Silva v138.1 n99 database. Samples were then rarefied to the minimum read count of the successfully amplified samples (51659 reads), and filtered based on at least 4 reads of a taxa present in 10% of samples. Visualization and analysis were carried out using MicrobiomeAnalyst [35], and the phyloseq R package [36].

When examining the microbial diversity of the microbial biofilms, we found them to be highly heterogeneous (Fig. 7) and dominated by heterotrophic mi-

Table 1: Table of parameters from a Logistic and Gompertz fit. The final level  $A$ , fouling rate  $k_{\text{foul}}$ , inflection time  $T_i$  and calculated critical time  $T_c$  of the two models after fitting. Time measurements are taken from the start of data taking, 8 months after the initial deployment.

Model	$A$	$k_{\text{foul}}$ (% yr $^{-1}$ )	$T_i$ (yr)	$T_c$ (yr)	p-value of fit
Logistic	$0.77 \pm 0.12$	$26.0 \pm 3.8$	$3.2 \pm 0.3$	$1.72 \pm 0.15$	0.92
Gompertz	$1.14 \pm 0.37$	$23.4 \pm 6.9$	$3.3 \pm 0.5$	$1.54 \pm 0.21$	0.98

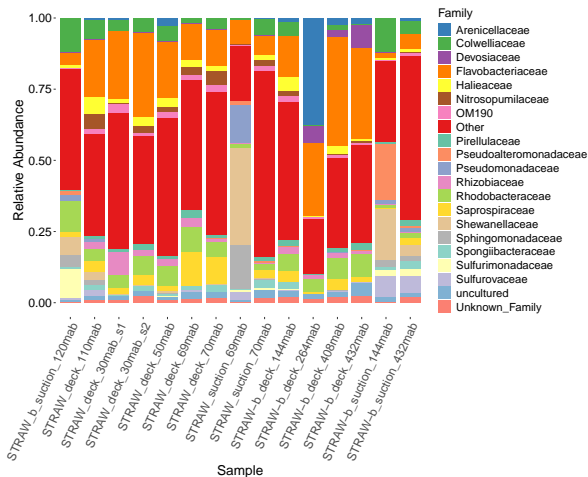


Fig. 7: Stacked bar plot showing the relative abundance of the 20 most abundant families of each successfully amplified sample collected for microbiome analysis from STRAW and STRAW-b. Sample names are labelled by the pathfinder apparatus (STRAW or STRAW-b), sampling technique (suction or deck), and the meters above the sea floor (e.g, 144mab). Two measurements (s1 and s2) are shown for the STRAW instrument at 30mab, as it was sampled on both the top and bottom surfaces.

crobes (Fig. 8). The most abundant taxa were members of the family Flavobacteriaceae (17%), rhodobacteriaceae (5%), colwelliaceae (5%), and shewanellaceae (5%) (Fig. 8); all of these families are largely heterotrophic, using organic matter from the environment to obtain their energy [37, 38, 39]. As the dominant form of food at these depths is sinking organic matter that accumulates on surface-facing surfaces, angling sensors and developing methods where particulates do not collect would likely reduce biofilm formation on the sensors. All PMTs on the P-ONE optical modules are angled away from the vertical, so we expect the impact of biofouling to be less than what we have presented here for the purely upward-facing STRAW modules. Additionally, a subset of modules on the first P-ONE string will be deployed with ClearSignal<sup>TM</sup> anti-biofouling coating, in order to test it's efficacy on upward-facing modules.

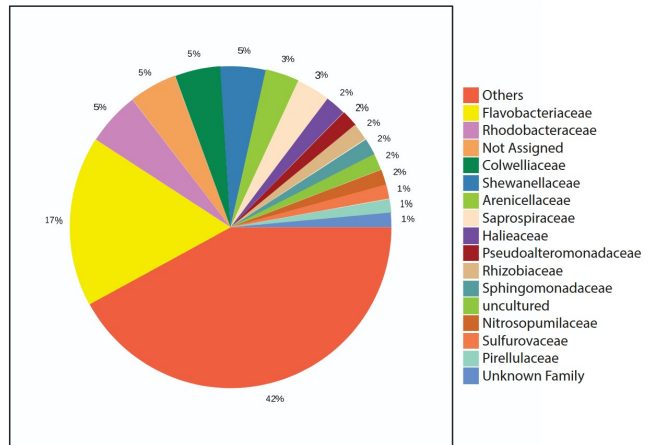


Fig. 8: Pie chart showing the relative abundance of the 15 most abundant bacterial and archaeal families across all successfully amplified samples. Families outside of the 15 most abundant are grouped into the ‘Others’ category. Samples were taken from both STRAW and STRAW-b modules across varying depths and sensor types.

## 5 Discussion

The full P-ONE detector will be made up of one kilometre tall mooring lines, instrumented with optical modules. Neutrino events will be reconstructed based on the Cherenkov light that these modules observe in the water. The efficiency of the detector is therefore tied to the light sensing efficiency of photo-detectors that make up the optical modules.

Four years of data from the P-ONE pathfinder was analyzed for indications that the transparency of the instrument's optical surfaces had changed. After around the two and a half year mark, the upward-facing glass rapidly became less transparent as shown in Fig. 6. This loss of efficiency is attributed to the effects of sedimentation and biofouling. The data available doesn't allow us to make a conclusion at what point this efficiency loss reaches equilibrium. Models motivated by relevant literature have been fit to the data and used to estimate the critical time and extrapolate a range for the final transmission efficiency. A scenario where the upward-

facing light sensors become completely obscured cannot be ruled out based on the results of this fitting. A survey of the STRAW apparatus prior to recovery suggests that downward-facing optical modules are much less affected by fouling, and in several cases showed none. The sensitivity of the full P-ONE detector to astrophysical sources will be dominated by up-going events, and therefore influenced primarily by partially downward-facing PMTs. For example, Ref. [40] used only up-going events in their analysis.

P-ONE-1, the first prototype line for the experiment, is currently under development. This instrument will have 16 PMT optical modules and instrument 1 km of the water column, allowing for more robust measurements of the effects of biofouling and sedimentation. Based on observations as part of this analysis and the pathfinder recovery, some design choices may already offer some mitigation against these effects. No P-ONE-1 optical modules will look directly up, which is expected to reduce the effect of marine snow and sedimentation.

The second pathfinder was surveyed by an ROV before recovery, three years after deployment, suggesting that the impact of fouling decreases with distance above the seafloor. This is likely due to decreased resuspension of organic and inorganic particulates, as well as some of the biofouling settling invertebrate larvae when moving away from the benthic boundary layer. However, during recovery of the STRAW-b instrumentation fouling accumulation could not be quantified directly, so this is based on the qualitative observations made both from the ROV surveying videos as well as in the laboratory aboard the ship. For future P-ONE moorings, only the module closest to the seafloor on each string will be at a depth comparable to the STRAW modules discussed in this work.

The microbial biofilms on the STRAW and STRAW-b optical modules aligns with biofilm community structure on the other researched deep-sea neutrino detector. The KM3NeT site in the Mediterranean Sea has much reduced surface seasonal variability in comparison to the Cascadia Basin site studied here, although they both share similar light attenuation characteristics at depth [7, 41], and yet had similar gross microbial biofilm composition [20, 42]. Both the KM3Net and the STRAW biofilms included dominant groups of Gammaproteobacteria, Alphaproteobacteria, and Bacteroidia (grouped into Flexibacter/ Cytophaga-Bacteroides in 2012). However, especially at shallower depths (yet still >1500m), there was a greater proportion of cyanobacteria in the Mediterranean than we observed in the present study. Overall, this high level of similarity is remarkable considering the significant advance in microbial characterization since the important work of Ref. [20]. This sup-

ports a commonality in microbial biofilm communities within deep sea habitats even on arrays on different sides of the planet and vastly different oceanography. This basic understanding of community composition further allows a more directed study on the rate of microbial growth of the taxonomic groups that form the biofilm. Growth rate studies based on this information can quantify a relationship between surface productivity, seasonality, and depth on the rate of biofilm formation since the general taxa appear, at least at a first order, to be similar across the oceans at these depths and instruments.

In order to maximize the long-term sensitivity of upward-facing light sensors, fouling mitigation strategies are being explored. Currently, the most favorable anti-fouling approach is a fouling release coating. This type of coating works by weakening the adhesion between biofouling organisms and the infrastructure, allowing for the removal of these organisms by ocean currents or other mechanical means [43, 44, 45]. The current industry standard is to use silicone based coatings which are commercially available and reduce biofouling population adhesion by up to 97% [46]. The ClearSignal (Ref. [47]) fouling release coating will be tested in Cascadia Basin by applying it to selected optical modules on P-ONE-1.

**Acknowledgements** We thank Ocean Networks Canada for the very successful operation of the NEPTUNE observatory, as well as the support staff from our institutions without whom this experiment and P-ONE could not be operated efficiently. We acknowledge the support of the Natural Sciences and Engineering Research Council of Canada (NSERC) and the Canadian Foundation for Innovation (CFI). This research was enabled in part by support provided by the BC and Prairies DRI and the Digital Research Alliance of Canada (alliancecan.ca). This research was undertaken thanks in part to funding from the Canada First Research Excellence Fund through the Arthur B. McDonald Canadian Astroparticle Physics Research Institute. P-ONE is supported by the Collaborative Research Centre 1258 (SFB1258) funded by the Deutsche Forschungsgemeinschaft (DFG), Germany. We acknowledge support by the National Science Foundation. This work was supported by the Science and Technology Facilities Council, part of the UK Research and Innovation, and by the UCL Cosmoparticle Initiative. This work was supported by the Polish National Science Centre (NCN).

## References

1. M. Agostini et al., *Nat. Astron* **4**, 913 (2020). <https://doi.org/10.1038/s41550-020-1182-4>
2. C. Barnes, M. Best, F. Johnson, L. Pautet, B. Pirenne, in *2011 IEEE Symposium on Underwater Technology and Workshop on Scientific Use of Submarine Cables and Related Technologies* (2011), pp. 1–7. <https://doi.org/10.1109/UT.2011.5774134>

3. M. Aartsen et al., *Science* **361**, aat1378 (2016). <https://doi.org/10.1126/science.aat1378>
4. R. Abbasi et al., *Science* **380**, 1338 (2023). <https://doi.org/10.1126/science.adc9818>
5. F. Halzen, *Eur. Phys. J. C* **46**, 669 (2006). <https://doi.org/10.1140/epjc/s2006-02536-4>
6. M. Boehmer et al., *JINST* **14**, P02013 (2019). <https://doi.org/10.1088/1748-0221/14/02/P02013>
7. N. Bailly et al., *Eur. Phys. J. C* **81**, 1071 (2021). <https://doi.org/10.1140/epjc/s10052-021-09872-5>
8. K. Holzapfel, *Bioluminescence in the Pacific Ocean Neutrino Experiment: Shedding Light on the Deep Sea 2023*. Ph.D. thesis, Technische Universität München (2023)
9. I. Rea et al., *PoS* **395**, 1092 (2021). <https://doi.org/10.22323/1.395.1092>
10. K. Hozapfel et al., *JINST* **19**, P05072 (2024). [10.1088/1748-0221/19/05/P05072](https://doi.org/10.1088/1748-0221/19/05/P05072)
11. F. Henningsen et al., *JINST* **16**, C09033 (2021). [10.1088/1748-0221/15/07/P07031](https://doi.org/10.1088/1748-0221/15/07/P07031)
12. U. Siegenthaler, J.L. Sarmiento, *Nature* **365**, 119 (1993). <https://doi.org/10.1038/365119a0>
13. J. Hedges, J. Oades, *Org. Geochem.* **27**, 319 (1997). [https://doi.org/10.1016/S0146-6380\(97\)00056-9](https://doi.org/10.1016/S0146-6380(97)00056-9)
14. S. Fowler, G. Knauer, *Prog. Oceanogr.* **16**, 147 (1986). [https://doi.org/10.1016/0079-6611\(86\)90032-7](https://doi.org/10.1016/0079-6611(86)90032-7)
15. A. Alldredge, M.W. Silver, *Prog. Oceanogr.* **20**, 41 (1988). [https://doi.org/10.1016/0079-6611\(88\)90053-5](https://doi.org/10.1016/0079-6611(88)90053-5)
16. N. Gule, N. Begum, B. Klumperman, *Crit Rev Environ Sci Technol* **46**, 535 (2016). <https://doi.org/10.1080/10643389.2015.1114444>
17. C. de Carvalho, *Front. Mar. Sci.* **5**, 126 (2018). <https://doi.org/10.3389/fmars.2018.00126>
18. P. Vuong, A. McKinley, P. Kaur, *npj Materials Degradation* **7**, 50 (2023). <https://doi.org/10.1038/s41529-023-00370-5>
19. P. Amram et al., *Astropart. Phys.* **19**, 253 (2003). [https://doi.org/10.1016/S0927-6505\(02\)00202-5](https://doi.org/10.1016/S0927-6505(02)00202-5)
20. N. Bellou, E. Papatthanassiou, S. Dobretsov, V. Lykousis, F. Colijn, *Biofouling* **28**, 199 (2012). <https://doi.org/10.1080/08927014.2012.662675>
21. M. Ageron et al., *Nucl. Instrum. Methods Phys. Res. a* **656**, 11 (2011). <https://doi.org/10.1016/j.nima.2011.06.103>
22. A. Alberta et al., *Eur. Phys. J. C* **78**, 669 (2018). <https://doi.org/10.1140/epjc/s10052-018-6132-2>
23. P. Amram et al., *Nucl. Instrum. Methods Phys. Res. a* **484**, 369 (2002). [https://doi.org/10.1016/S0168-9002\(01\)02026-5](https://doi.org/10.1016/S0168-9002(01)02026-5)
24. I. Rea, *The Pacific Ocean Neutrino Experiment: feasibility study for a new Neutrino Telescope at Cascadia Basin, NE Pacific Ocean*. Ph.D. thesis, Technische Universität München (2021)
25. P. Hatch, K. Holzapfel, L. Ruohan, C. Spannfellner, B. Veenstra, *PoS* **444**, 1166 (2023). <https://doi.org/10.22323/1.444.1166>
26. M. Agostini et al., *JINST* **20**, P07003 (2025). <https://doi.org/10.1088/1748-0221/20/07/P07003>
27. M. Suckow, S. Weisbroth, C. Franklin, in *Seawater (Second Edition)* (Butterworth-Heinemann, 1995), pp. 61–84. <https://doi.org/10.1016/B978-075063715-2/50006-X>
28. D. Charlebois, G. Balázs, *In Silico Biology* **13**, 21 (2019). <https://doi.org/10.3233/ISB-180470>
29. E. Tjørve, K.M.C. Tjørve, *Journal of Theoretical Biology* **267**, 417 (2010). <https://doi.org/10.1016/j.jtbi.2010.09.008>
30. K.M.C. Tjørve, E. Tjørve, *PLOS ONE* **12**, e0178691 (2017). <https://doi.org/10.1371/journal.pone.0178691>
31. Emp. <https://github.com/biocore/emp>
32. A. Thurber, S. Seabrook, R.M. Welsh, *Proc. R. Soc. B: Biol. Sci.* **287**, 20201134 (2020). <https://doi.org/10.1098/rspb.2020.1134>
33. S. Chen, *iMeta* **2**, e107 (2023). <https://doi.org/10.1002/imt2.107>
34. M. Estaki et al., *Curr. Bionform.* **70**, e100 (2020). <https://doi.org/10.1002/cpbi.100>
35. J. Chong, P. Liu, G. Zhou, J. Xia, *Nat. Protoc.* **15**, 799 (2020). <https://doi.org/10.1038/s41596-019-0264-1>
36. P. McMurdie, S. Holmes. *phyloseq: An R package for reproducible interactive analysis and graphics of microbiome census data* (2013). <https://doi.org/10.1371/journal.pone.0061217>
37. J.P. Bowman, *The Family Colwelliaceae* (Springer Berlin Heidelberg, Berlin, Heidelberg, 2014), pp. 179–195. [https://doi.org/10.1007/978-3-642-38922-1\\_230](https://doi.org/10.1007/978-3-642-38922-1_230)
38. S. Chen, Y. Ding, *FEMS Microbiol. Ecol.* **99**, fiad124 (2023). <https://doi.org/10.1093/femsec/fiad124>
39. X. Xia et al., *Sci. Total Environ.* **798**, 149208 (2021). <https://doi.org/10.1016/j.scitotenv.2021.149208>
40. R. Abbasi et al., *Science* **378**, 538 (2022). <https://doi.org/10.1126/science.abg3395>
41. G. Riccobene et al., *Astropart. Phys.* **27**, 1 (2007). <https://doi.org/10.1016/j.astropartphys.2006.08.006>
42. N. Bellou, F. Colijn, E. Papatthanassiou, *Nucl. Instrum. Methods Phys. Res. A* **626-627**, S102 (2011). <https://doi.org/10.1016/j.nima.2010.04.131>
43. J. Finlay, M. Schultz, G. Cone, M. Callow, J. Callow, *Biofouling* **29**, 401 (2013). <https://doi.org/10.1080/08927014.2013.777046>
44. M. Lejars, A. Margaillan, C. Bressy, *Chem. Rev.* **112**, 4347 (2012). <https://doi.org/10.1021/cr200350v>
45. H. Peng, Q. Xie, C. Ma, G. Zhang, *Langmuir* **36**, 2170 (2020). <https://doi.org/10.1021/acs.langmuir.9b03926>
46. H. Lobe, in *OCEANS 2015 - MT-S/IEEE Washington* (2015), pp. 1–4. <https://doi.org/10.23919/OCEANS.2015.7401854>
47. Clearsignal. <https://clearsignalcoating.com/>